The crystal orientation of THF clathrates in nano-confinement by in-situ polarized Raman spectroscopy

Journal:	*Lab on a Chip*
Manuscript ID	LC-ART-10-2023-000884.R1
Article Type:	Paper
Date Submitted by the Author:	19-Dec-2023
Complete List of Authors:	Sharma, Mrityunjay; New York University Tandon School of Engineering, Department of Chemical and Biomolecular Engineering Leong, Xin Ning; New York University, Department of Chemical and Biomolecular Engineering Koh, Carolyn; Colorado School of Mines, Chemical Engineering Department Hartman, Ryan; New York University, Department of Chemical and Biomolecular Engineering

ARTICLE

The crystal orientation of THF clathrates in nano-confinement by *in-situ* polarized Raman spectroscopy

Received 00th January 20xx,
Accepted 00th January 20xx

DOI: 10.1039/x0xx00000x

Mrityunjay K. Sharma[a], Xin Ning Leong[a], Carolyn A. Koh[b], Ryan L. Hartman[a*]

Gas hydrates form at high pressure and low temperatures in marine sediments and permafrost regions of the earth. Despite forming in nanoporous structures, gas hydrates have been extensively studied only in bulk. Understanding nucleation and growth of gas hydrates in nonporous confinement can help create ways for storage and utilization as a future energy source. Herein, we introduce a new method for studying crystal orientation/tilt during Tetrahydrofuran (THF) hydrate crystallization under the influence of nano-confinement using polarized Raman spectroscopy. Uniform cylindrical nanometer size pores of Anodic Aluminum Oxide (AAO) are used as a model nano-confinement, and hydrate experiments are performed in a glass microsystem for control of the flash hydrate nucleation kinetics and analysis *via in-situ* Polarized Raman spectroscopy. The average THF hydrate crystal tilt of 56±1° and 30.5±0.5° were observed for the 20nm and 40nm diameter pores, respectively. Crystal tilt observed in 20 and 40-nanometer-size pores was proportional to the pore diameter, resulting in lower tilt relative to the axis of the confinement at larger diameter pores. The results indicate that the hydrates nucleation and growth mechanism can depend on the nanoconfinement size. A 1.6±0.01°C to 1.8±0.01°C depression in melting point compared to the bulk is predicted using the Gibbs-Thomson equation as a direct effect of nucleation in confinement on the hydrate properties.

1 Introduction

Gas hydrates are nanometer-size crystalline inclusion compounds where small guest molecules occupy cages formed by hydrogen-bonded host molecules[1]. The type of guest molecule (e.g., methane, ethane, sulfur dioxide, carbon dioxide, etc.) and the size of the cavities of the guest molecules (e.g., water) dictates the size of hydrates[1, 2]. Three main structures, cubic structure I (sI), cubic structure II (sII), and hexagonal structure (sH), have been identified for the Gas Hydrates depending on temperature, pressure, size, and type of guest molecule[1-4]. High energy density, less environmental impact, and availability in enormous quantities make methane hydrates a future clean energy source, which resulted in numerous research and development activities in energy and environmental science[5-7]. Enormous accumulation volume is also a driver for understanding the potential role of hydrates as a geologic hazard and an agent of global climate change[8]. Methane hydrates have been studied as a static deposit for understanding the role of temperature-pressure conditions, gas source migration, and the presence of suitable reservoirs for hydrate formation; however, understanding in terms of geologic hazards and a climate change agent is still incomplete[9]. Also, understanding the kinetics of hydrate formation, nucleation, and growth phenomena of hydrates is essential for developing commercially viable technologies around Gas Hydrates[10-13]. Hydrate formation is a nucleation and growth phenomenon that occurs at specific temperature and pressure conditions[14, 15]. In nature, hydrates are abundant in marine sediments and permafrost in confined nanoporous spaces[16-19]. It has been shown that most methane hydrates are found at shallow depths in sand reservoirs which are primary targets for energy recovery, posing a challenge in terms of understanding the operational geohazard while drilling operations and well installation which can cause hydrate dissociation and subsequent release in the environment with various types of methane hydrate occurrences in nature[20]. It has been estimated that up to two percent of methane may originate through methane hydrate dissociation, prone to future warming scenarios[21]; however, the nature, mechanism, and extent of methane escape due to perturbations are poorly understood. While most hydrates form in confined media (sand reservoirs), they are extensively studied only in bulk as a static system ignoring the effect of confinement on hydrate nucleation, stability, dissociation kinetics, and phase behavior as a dynamic system. Understanding the hydrate nucleation and growth kinetics, dissociation kinetics and phase behavior in confinement will help in efficient and safe hydrate resource utilization by developing the technologies around vast reserves of methane hydrates around the world.

Only a few studies have been done to mimic nanoporous marine environments, e.g., using porous micromodels[22-25], millimeter-size plastic tubes[26, 27], submillimeter capillary tubes[28-30], etc., to

---

[a] *Department of Chemical & Biomolecular Engineering, NYU Tandon School of Engineering, Brooklyn, NY, USA 11201.*

[b] *Center for Hydrate Research, Department of Chemical & Biological Engineering, Colorado School of Mines, Golden CO, USA 80401*

Electronic Supplementary Information (ESI) available: [details of any supplementary information available should be included here]. See DOI: 10.1039/x0xx00000x visualize hydrate formation and understand crystallization and memory effect. Various materials, such as silica gel[31, 32], porous glass[33], graphene oxide[34], sand[35], clay[36], etc., have also been used to understand the effect of confinement on hydrate kinetics. It has been illustrated that confinement and the phase behavior of water at the nanoscale may affect the hydrate crystallization kinetics. However, the systems utilized are non-uniform with respect to the porosity and pores alignment. It is challenging to explore nucleation and growth mechanisms in confinement using standard microscopic visualization methods concerning hydrate formation conditions. Various phenomenological models have been developed based on observed data. Nevertheless, the results are scattered and lack the prediction ability due to model oversimplification in terms of pore habits, distribution in models, and complex geometries of pores in the presence of hydrates.

The confinement effect on crystal nucleation and growth has been well documented in various fields, e.g., pharmaceuticals, protein crystallography, nucleation kinetics, polymer crystallization, ice nucleation, nanomaterial synthesis, etc[37-39]. Isolated droplets, cylindrical pores in Anodic Aluminum Oxide, wedge-shaped pockets formed at the step edge in mica, etc.[40-42], can be used as the confining medium. While material transport in confinement can vary significantly compared to the bulk, confinement can dramatically affect the crystal morphologies, orientation, freezing and melting points, and nucleation rates. For a given confinement volume and geometry of confinement, the interfacial energy between the confinement medium and crystal dictates the observed effect, and it can be both thermodynamic and kinetic in origin. The ability to analyze crystals, either ex-situ or in-situ, is crucial for understanding crystallization under confinement. Various methods, such as microscopy, tomography-based methods, calorimetry, Nuclear Magnetic Resonance, X-ray diffraction, and neutron diffraction, can be employed based on the scale, confinement medium, and crystal properties. In general, applying these methods for crystals stable under atmospheric conditions is very helpful for generating insights about crystal behavior under confinement. Crystallization under high-pressure and low-temperature conditions, such as hydrates, specifically designed experimental systems with in-situ analytical techniques becomes crucial. One such method for determining crystal orientation is Polarized Raman Spectroscopy[43]. Polarized Raman Spectroscopy is an old and specialized technique utilized only for specific applications such as determining molecular orientation[44-46] and crystal axis[47] etc., for solids and molecules in liquid under confinement[43, 48-52]. However, it has never been used to study the crystals stable at low temperatures and high-pressure conditions in enclosed environment which is predominant in systems such as hydrates. Using this technique along with microsystems will open whole new area of application for Polarized Raman Spectroscopy for in-situ analysis of unstable systems or system stable under specific conditions of temperature and pressure in an enclosure.

The theory of Polarized Raman spectroscopy is well-developed and implemented for various crystal classes[53, 54]. It is possible to distinguish between allotropes and polymorphs[55-58], to identify vibrational modes[58], and to identify the polycrystalline material and orientation of crystal[51, 59, 60] and degree of disorder[61, 62] using this technique. It can also be used for in-depth non-contact analysis of crystalline samples for crystallographic measurement at the film or substrate interface. Raman spectra provide information about the sample's molecular structure that can be exploited to get the orientation of the crystal with reference to the highly ordered systems. Most liquids, powders, and randomly oriented polymers that are isotropic are not sensitive to the polarized light and cannot be used for orientation determination using Polarized Raman. However, even simple crystals are very sensitive to polarized light, and this technique can determine the orientation. Polarized Raman Spectroscopy is useful in determining the symmetry and orientation of the crystal because it depends on the polarization and direction of the incident light, which can be easily controlled and exploited for the range of systems and crystals[52]. In cases where samples are enclosed, techniques like polarized Raman spectroscopy have been shown to work efficiently to get the orientation of crystals inside the confinement. The alignment of the crystal axis relative to the polarization of the laser results in different spectra, which can be quantified to get the orientation of the crystal in 3D space.

With efficient control over parameters, optimum transport rates, and seamless integration of in-situ analysis techniques, microfluidic microsystems has been used for scientific and industrial research in almost every area of science in recent decades[63-66]. Especially droplet microfluidics[67] and thermally cooled microreactors[68, 69] have been employed for gas hydrate research. However, studied gas hydrates are in plane surfaces, and an understanding of pore-level confinement is missing. In the past, we have used microfluidics with integrated Raman spectroscopy to understand methane hydrate kinetics[68]. Understanding the confinement effect using microfluidic microsystem with in-situ Polarized Raman spectroscopy can lead to nanoscale insights that can help design better technologies and utilization strategies for the gas hydrates with strategies to mitigate the impact on the environment due to hydrate dissociation and emission from hydrate reserves. It has been shown that though THF and methane hydrates are different, THF can be a substitute for laboratory studies of methane hydrates[70]. Since THF hydrates form at moderate conditions, studies for the THF hydrates can be used to forecast the issues regarding the analysis of Methane hydrates. Accordingly, in the present work, we have used THF hydrates as a test case for understanding the nanoporous confinement effect on the hydrate crystallization and crystal orientation using Polarized Raman spectroscopy. Our results broadly impact the behavior of clathrates nucleated within nano-confinement.

2 Experimental

2.1 Polarized Raman spectroscopy theory

The irreducible representation of the space group of the crystal lattice is the result of the different symmetry of vibration in a crystal corresponding to the different phonon branches. By using standard group theoretical methods and the interaction of crystal with polarized light, we can determine the Raman active phonon modes of the crystal. When a material interacts with linearly polarized light, the interactions are different compared to the interaction with depolarized light, and the orientation of the sample can be determined based on how the axis of the material is aligned to the axis of the light. In this context, collecting the polarized Raman spectra for known crystallographic orientations can result in the symmetric properties of the phonon vibrations.

The incident laser beam of electric field E can induce polarization P in the material medium, which can be written as[53]

$$\mathrm{P} = \varepsilon_0 . \chi . \mathrm{E} \qquad (1)$$

Where, ε_0 is the electric permittivity of free space, and χ is the second-rank tensor electric susceptibility that accounts for the fact that vectors P and E are not necessarily parallel.

Raman intensity I of the light polarized along the direction of the unit vector e_i and when observed in the direction of the scattered unit vector e_s is proportional to[53]

$$I \propto | e_i R e_s |^2 \qquad (2)$$

R is the second-rank Raman tensor, specific to each Raman active phonon, and varies with the crystal structure. The Raman tensor is symmetric, so only six independent elements need to be considered for analysis. The proportionality accounts for the intensity dependence on the instrumental parameters, such as the numerical aperture of the objective, efficiency of the spectrometer, intensity of the incident light, etc. For parallel polarized incident light, both parallel and cross-polarization geometry of scattered light is possible, and the polarization vectors can be written as[53]

$$e_i^{\parallel} = \begin{pmatrix} 0 & 1 & 0 \end{pmatrix} \qquad (3)$$

$$e_s^{\parallel} = \begin{pmatrix} 0 \\ 1 \\ 0 \end{pmatrix} \qquad (4)$$

$$e_s^{\perp} = \begin{pmatrix} 1 \\ 0 \\ 0 \end{pmatrix} \qquad (5)$$

Where subscript i and s refer to the incident and scattered light and superscript ∥ and ⊥ refers to parallel and cross-polarization configurations, respectively. The Raman tensor can give the orientation of the crystal with reference to the cartesian system associated with the crystal frame. However, a transformation matrix is needed to get the coordinates associated with the laboratory frame.

$$R_{xyz} = \Phi_{xyz} \, R \, \Phi'_{xyz} \qquad (6)$$

The matrix of Euler angles is used for these purposes, where the transformation matrix of Euler angles. Φ_{xyz} and its inverse Φ'_{xyz} is defined as[71]

$$\Phi_{xyz} = \begin{bmatrix} cos\theta cos\varphi cos\psi - sin\varphi sin\psi & cos\theta sin\varphi cos\psi + cos\varphi sin\psi & -sin\theta cos\psi \\ -sin\varphi cos\psi - cos\theta cos\varphi sin\psi & cos\varphi cos\psi - cos\theta sin\varphi sin\psi & sin\theta sin\psi \\ sin\theta cos\varphi & sin\theta sin\varphi & cos\theta \end{bmatrix} \qquad (7)$$

$$\Phi'_{xyz} = \begin{bmatrix} cos\theta cos\varphi cos\psi - sin\varphi sin\psi & -sin\varphi cos\psi - cos\theta cos\varphi sin\psi & sin\theta cos\varphi \\ cos\theta sin\varphi cos\psi + cos\varphi sin\psi & cos\varphi cos\psi - cos\theta sin\varphi sin\psi & sin\theta sin\varphi \\ -sin\theta cos\psi & sin\theta sin\psi & cos\theta \end{bmatrix} \qquad (8)$$

Here, $0 \le \theta \le \pi$, $0 \le \varphi \le 2\pi$, and $0 \le \psi \le 2\pi$.

The Raman polarizability tensor depends on the position of atoms and directions of bonds in a molecule. So, for crystals fixed in space the Raman tensor can describe the crystal symmetry and orientation relative to the direction and polarization of the incident and collected light. Using the Raman tensor pertaining to the unique crystal structure, it is possible to obtain the series of independent equations which can be used to investigate the crystallographic plane and for the determination of the orientation of crystal in space. For 32 crystal classes, the Raman tensor forms have already been determined and tabulated in literature. THF hydrate crystals are octahedral, belonging to the ***O_h*, *m3m*** point, and ***Fd3m*** space groups[72]. The Raman tensor for this crystal class is given as[53]

$$R_{A_{1g}} = \begin{bmatrix} a & 0 & 0 \\ 0 & a & 0 \\ 0 & 0 & a \end{bmatrix} \qquad (9)$$

$$R_{E_g} = \begin{bmatrix} b & 0 & 0 \\ 0 & b & 0 \\ 0 & 0 & -2b \end{bmatrix}, \begin{bmatrix} -\sqrt{3b} & 0 & 0 \\ 0 & \sqrt{3b} & 0 \\ 0 & 0 & 0 \end{bmatrix} \qquad (10)$$

$$R_{F_{2g}} = \begin{bmatrix} 0 & 0 & 0 \\ 0 & 0 & d \\ 0 & d & 0 \end{bmatrix}, \begin{bmatrix} 0 & 0 & d \\ 0 & 0 & 0 \\ d & 0 & 0 \end{bmatrix}, \begin{bmatrix} 0 & d & 0 \\ d & 0 & 0 \\ 0 & 0 & 0 \end{bmatrix} \qquad (11)$$

Here, the vibration fundamentals for the A_{1g}, E_g, and F_{2g} modes can be determined by changing the instrument configuration during spectrum acquisition described by Porto notation[73].

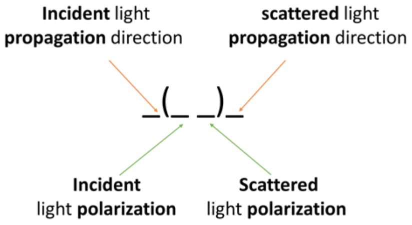

Figure 1. Porto notation for the instrument configuration

According to Porto notation (**Fig. 1**), Z(XY)Z means the incident laser propagated along Z-axis, polarized along X-axis, and scattered light polarized along Y-axis propagated along Z-axis (called backscattering mode) was acquired. According to this notation, four possible configurations of the instrument are possible where Z(XX)Z and Z(YY)Z are considered parallel configurations and Z(XY)Z and Z(YX)Z a cross configuration. As each irreducible representation in each crystal class has a tensor of specific form with respect to the crystallographic axes, the parallel configuration will only yield A_{1g} modes, and the cross configuration will yield E_g modes. For polarized Raman, the determination of Raman tensor elements is an important criterion deduced by performing the angle-resolved experiments where the direction of the incident and scattered light is continuously changed with respect to crystallographic axes. The Raman tensor is unique for each Raman-active mode, and the given peak intensity can be characterized as a function of incident and scattered polarization. Accordingly, substituting **eqn. (3-8)** into **eqn. 2** form **eqn. (12-13)** for experiments performed in parallel and cross configurations.

$$I_{\parallel} \propto |\begin{pmatrix}0 & 1 & 0\end{pmatrix} \Phi_{xyz}\, R\, \Phi'_{xyz} \begin{pmatrix}0\\1\\0\end{pmatrix}|^2 \tag{12}$$

$$I_{\perp} \propto |\begin{pmatrix}0 & 1 & 0\end{pmatrix} \Phi_{xyz}\, R\, \Phi'_{xyz} \begin{pmatrix}1\\0\\0\end{pmatrix}|^2 \tag{13}$$

The angle-resolved experiments can be performed by either fixing the analyzer in parallel or perpendicular positions to the fixed incident polarization while the sample is rotated.

2.2 Glass microsystem fabrication

A simple modified glass etching technique is used to create micron-scale square depth onto a precut borosilicate glass slide. The slide is covered on both sides with acid-resistant tape, and a 3 mm square area on one side is carved out for the acid etching to create a depth of micrometer size. The slide is placed in the Hydrofluoric acid solution (50% wt./vol.) for 1 hour to etch at a depth of 250 micrometers. This etch cavity is a microsystem used in the study presented in the manuscript. While performing experiments AAO wafer (InRedox LLC, USA) with a known pore diameter (20, 40 nanometer) is placed inside the cavity, which is then filled with THF water mixture (1:17 mol/mol) covered with the 100-micrometer thick soda lime glass coverslip with the help of the regular tape. (**Fig. 2**).

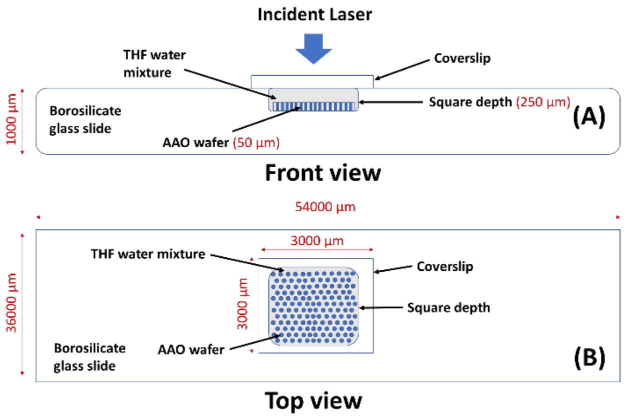

Figure 2. (A) Side view and (B) top view of the Anodic Aluminum Oxide nanopores placed in the microsystem made in borosilicate glass

2.3 Microsystem assembly

Inhouse-designed microsystem assembly in the lab was used with slight modification per the current experimental needs[68]. The assembly contains a previously used thermoelectric cooling system for stepwise temperature changes and isothermal operation. Air-assisted cooling used in the past is replaced with the liquid cooling system as these experiments demanded cooling below subzero temperatures. Stainless-steel compression chucks were used for holding the microreactor in place while measurement of data during rotational experiments. A thermoelectric module (TEC, TE Technology HP-127-1.4-1.5-74, max. 65 W) is used for cooling the microreactor base, which is in direct contact with the cooling side of the thermoelectric module with a silicon piece sandwiched in between. The silicon piece assists in clear observation inside the square depth during experiments. The maximum cooling rate possible is 1.05 K s-1. The device's temperature is monitored using a thermistor (TE Technology MP-2444) and controlled by a PID controller (TE Technology RS485). The hot side of the thermoelectric module is attached to the small aluminium reservoir, with cold water (5°C) circulation acting as a heat sink through the thermal paste (**Fig. 3**). The assembled microreactor system is placed inside the class 1 laser enclosure for in-situ Polarized Raman spectroscopy.

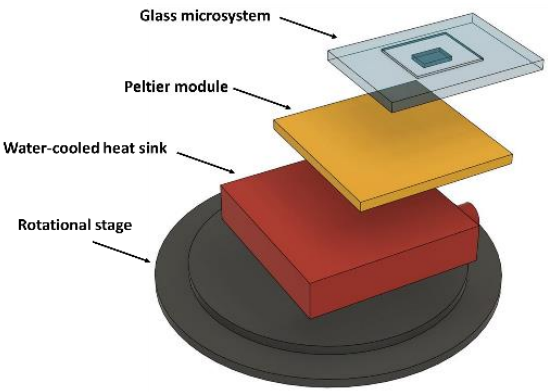

Figure 3. Experimental assembly including a rotational stage for angle-resolved experiments, heat sink, thermoelectric module (Peltier) for the temperature control and glass microsystem

2.4 Hydrate formation and dissociation

Before cooling the systems for hydrate formation, the Raman microscope is focused inside the microreactor, and a spectrum is acquired to confirm the THF and water peaks in bulk (**Fig. 4A**). The microreactor is cooled to -10°C at 1°C/min^{-1}. After this point, the temperature is reduced to 1°C every 10 min to monitor the hydrate formation in the microreactor. Going below 0°C creates the issue of moisture condensation on the cover slip forming ice below -4°C, which hinders the visuals from the confocal microscope inside the microreactor. To avoid moisture condensation, the surface of the microreactor was continuously flushed with in-house dry air **(SI)**. However, this results in a temperature gradient in the microreactor, which is recorded with the help of an IR camera **(SI)**. The confirmatory Raman spectrum is acquired in the bulk of the hydrates after visual confirmation of the hydrates in the microreactor (**Fig. 4B**). To melt the formed ice along with hydrates during cooling process inside microreactor, the temperature is raised to -10°C at 1°C/min^{-1} and then 1°C every 10 min until ice melting is observed. Confirmatory Raman spectrum is acquired for the hydrates with no ice (**Fig. 4C**), and the system is maintained at this temperature for 1 hour for hydrates stabilization before starting the rotational measurements.

It is established that the most prominent modes in pure THF are at 916 and 1034 cm^{-1} (**Fig. 4**). The stronger mode at 916 cm^{-1} was earlier assigned to C–C–C–C stretching (ring breathing) mode, and the weaker mode at 1031 cm^{-1} was attributed to C–O–C stretch. The mode at 916 cm^{-1} is degenerated, which showed splitting (920; 891 cm^{-1}) in an aqueous mixture of THF. The Raman spectrum in hydrate form shows a distinctly different spectrum, as shown in Figure 4, wherein the band due to C–C–C–C stretching degenerated at 922 cm^{-1}. These results broadly agree with earlier reports. For the scope of understanding we have focused on the 922 cm^{-1} peak only, the other peaks in the spectra are noise, and were not considered during analysis. OH, stretching in water appears at 3385 cm^{-1} whereas rise in intensity at 3135 cm^{-1} shows phase transition of water to ice.

2.5 Rotational measurement using polarized Raman spectra

For angle-resolved measurement, the reactor assembly (**Fig. 3**) (microreactor, thermoelectric module, aluminium heat sink) is mounted on the rotational stage (Thor labs.) for 360° rotation of the microreactor, i.e., the crystals. The spectrum is acquired for every 10° increment in rotation till 180° and then rotated back to the starting position resulting in 2 measurements at each rotation angle. The attached tube for the cold-water supply in the aluminium heat sink obstructs the full 360° rotation. Hence only 180° rotation is performed, and the intensity value is extracted for each collected Raman spectrum. The obtained intensity with respect to the stage rotation is used for getting the crystal tilt inside the nanopores. The angular dependence of the intensity of the Raman bands was fitted to theoretical equations according to the least-square method.

2.6 Raman instrument configuration

The Polarized Raman spectra for the THF hydrate crystals are collected using in situ confocal Raman spectroscopy (Horiba LabRam HR evolution, Jobin-Yvon) equipped with charged coupled detector camera and sheets of polarization filters. Diode-Pumped Solid-State (DPSS) laser system emitting light at 532 nm and 785 nm is used for the spectrum acquisition. The laser power is calibrated before spectrum acquisition to ensure that hydrate crystals are not dissociating during measurement. CCD Synapse EM detector is used to acquire the spectra with a grating of 600 grooves per mm. Spectra are fitted according to the mixed Gaussian/Lorentzian peak functions after subtracting a linear baseline with commercial software Labspec 5.6, Horiba/Jobin-Yvon, Kyoto, Japan.

3 Results and discussion

A laser wavelength of 532nm gives sharp Raman signature shifts at 922 cm^{-1} to identify the transformation of THF water mixture to THF hydrates. The acquired signal can distinguish between the presence of THF hydrates and ice or water (**Fig. 4**). However, the signal disappears when the 532 nm wavelength is used for THF hydrates in AAO nanopores. It was observed that at this wavelength, AAO wafer results in a large amount of fluorescence which saturates the spectrum, which is difficult to convolute even at very low laser power. Given the high tolerance of 785 nm laser for fluorescence, a good quality spectrum can be acquired for THF. However, using a 785 nm laser, only THF bands are visible, and OH bands do not appear in the spectrum (**Fig. 5**)[74]. So, to confirm THF hydrate crystals in water, we relied on the 532 nm laser, and the angle-resolved measurements were switched to the 732 nm laser. As performing the angle-resolved measurements involves acquiring the spectra at one location, there is a possibility of crystal melting over repeated irradiation if the power of the laser is too high. To perform the experiments in the crystal stability limit of the THF hydrates, the power of both lasers was measured using an optical power meter for two objectives and varying exposure (**SI**).

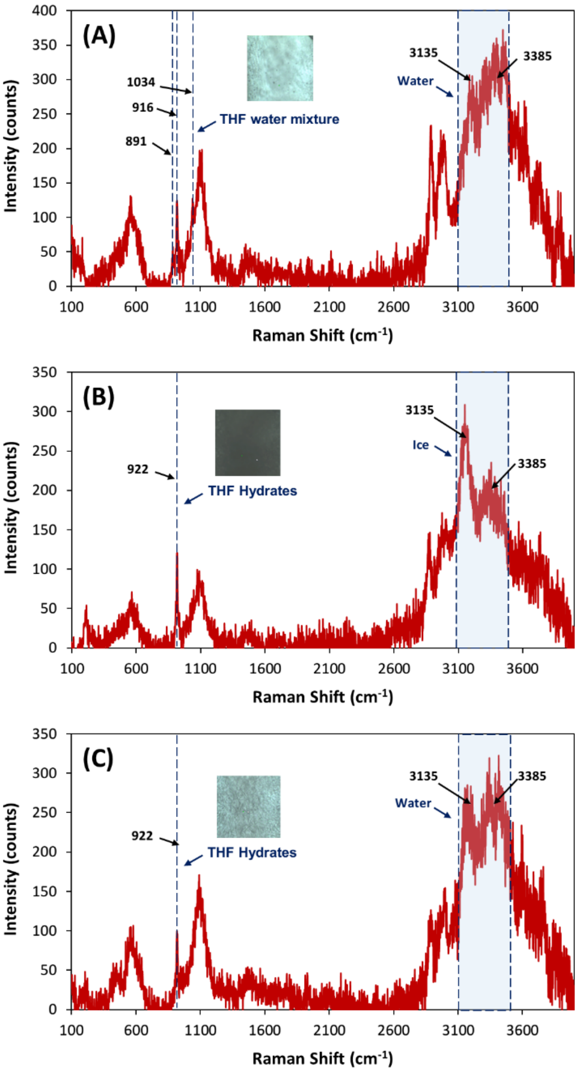

Figure 4. Monitoring the transformation of Aqueous THF (THF + water) to THF hydrates via rapid subcooling using 532nm laser; Raman spectra of (a) aqueous THF at 6°C; (b) THF hydrates and Ice formed at subcooling of 16°C; (c) THF hydrates with water at subcooling of 1°C (THF water mixture Raman shift = 891, 916, 1034 cm^{-1}, THF hydrate Raman shift = 922 cm^{-1}, water OH stretching = 3385 cm^{-1}, characteristic ice transformation = 3135 cm^{-1})

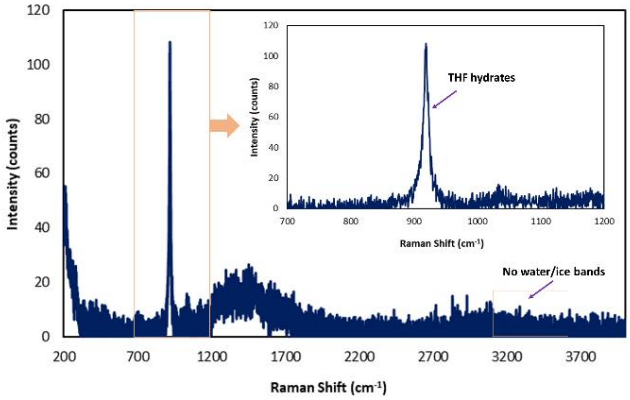

Figure 5. THF hydrates signal acquired using 785nm laser. Water/Ice shifts do not show up in the acquired spectrum (THF hydrate Raman shift = 922 cm^{-1})

The pore size distribution of marine sediments depend on the mineral and organic matter of the sediments. The sediments with more organic contents contain more heterogeneous and complex structures. The characteristics of the marine sediments have been studied with different characterization techniques, e.g., XRD, N_2 adsorption, FE-SEM, etc., and the properties of the pores have been determined. The pore size of the sediments falls in the mesoporous range from 2nm to 50nm, mostly averaging around 20nm for variety of marine sediments. Also, researchers have tried to mimic marine sediments with various materials (mentioned in introduction) averaging the pore size of ~20 nm. The 20nm and 40nm diameter AAO pores were chosen such that the results obtained can be broadly applied and comparable to the hydrates formed in marine sediments. In the present study (**Table 1**), as the AAO wafer thickness was 50 micrometers with varying interpore distance (pore density), the depth at which good quality spectral resolution can be obtained varied and determined before each analysis **(SI)**.

Table 1. AAO wafer properties and signal acquisition depth

Pore diameter (nm)	Thickness (µm)	Pore density (cm^{-2})	Porosity (%)	Signal acquisition depth from the surface of the AAO (µm)
20 ± 3	50 ± 5	5.8×10^{10}	12 ± 2	40
40 ± 4	50 ± 5	1×10^{10}	12 ± 2	20

3.1 Signal acquisition modes

Though cubic crystal is optically isotropic, the directional properties of the lattice waves result in the change in the Raman spectrum based on the orientation of the crystallographic axes to the direction and polarization of exciting radiation[52]. The forms of the Raman Tensor for the THF octahedron crystal are given in **eqn. (9-11)**. Different instrument configurations are possible for the experiment, and each will result in different vibrational fundamentals of the crystals. To get the crystal orientation using polarized Raman spectroscopy, it is necessary to determine the tensor element through angle-resolved experiments using a single crystal. It is very challenging to isolate the single crystal for the scope of Raman analysis using techniques mentioned in the literature for observing the nucleation and growth inside the bulk volume of the THF water mixture through seeding using the metal wire. As it has already been identified that THF hydrates form octahedral crystals, we formed THF hydrates inside a petri dish on the Raman rotation stage, and the crystals were allowed to grow very slowly. The petri dish was scanned through Raman microscope for the sufficiently large crystal, and a Raman signal was acquired at one of the visible faces of the crystal (**Fig. 8**). Initially, the Raman signal was acquired for four different instrument configurations (as mentioned previously) (Z(YY)Z, Z(XY)Z, Z(XX)Z, and Z(YX)Z) to check the instrument response and nature of the Raman bands on a crystal face under observation. To our surprise, Raman bands for THF hydrates and Ice crystals were observed only in a parallel configuration (Z(YY)Z and Z(XX)Z). In contrast, cross configuration (Z(XY)Z and Z(YX)Z) resulted in no noticeable peaks.

The crystal was fixed in these experiments, and laser polarization was changed using a half-wave plate. In general, the instrument laser is polarized along the Y-axis, and for changing the polarization along the X-axis half-wave plate was used. The signal obtained in the parallel configuration where laser polarization is along Y-axis was an exact multiple of when the laser is polarized along the X-axis. This can be attributed to the sensitivity of grating, which is sensitive to laser polarization. However, the fact that the signals were in exact multiple when the laser polarization axis was changed dictates that the signal acquisition in only one parallel configuration is sufficient to analyze the crystal tilt. This is advantageous in two ways, (i) As cross configuration does not result in any peaks at all, E_g modes are inactive, and tensor elements for E_g modes are not desired; (ii) As data acquired in one Y-parallel configuration is the exact multiple of the X-parallel configuration, angle-resolved experiments can be performed in only one laser polarization which reduces significant experimental labor and instrument calibration requirements. Also, except E_g modes, A_{1g} and F_{2g} modes contain the same tensor elements; it can be treated as constant for calculation purposes, and data obtained through angle-resolved experiments can be directly used for curve fitting of the derived expressions, and crystal orientations can be obtained. It is recognized that THF molecules in hydrate cages feel the same force field as the neat liquid. The energy of C-C-C-C stretching almost coincides with C-O-C + CH_2 modes resulting in the symmetric peak, which is observed as degenerate modes[75]. This information suggests using F_{2g} modes for curve fitting to the obtained data. Also, as the free rotation of the guest THF molecules in the hydrate cages are restricted by the weak guest host hydrogen bond at low temperature[75] may have resulted in a spectrum in only one configuration. Raman spectrum with all four configurations was acquired for the different faces of the THF hydrates crystal, and the same results were obtained (**Fig. 8**). Raman tensor for A_{1g} and F_{2g} modes contains the same elements, which can be taken as constant, and equations can be formulated for curve fitting for the data obtained for AAO nanoconfinement[51].

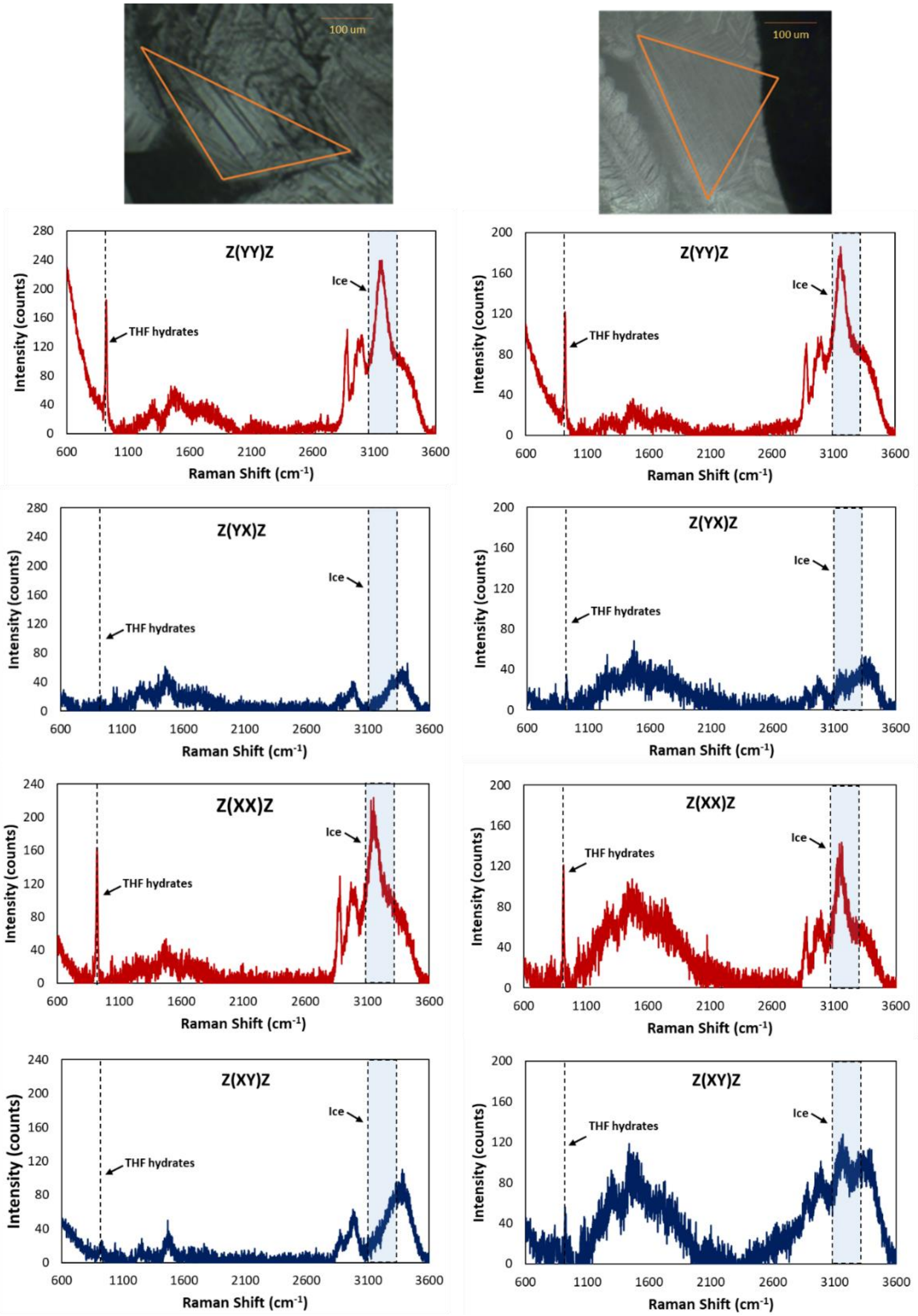

Figure 6. Observed Raman spectrum in parallel and crossed configurations at two different (1,1,1) faces of THF hydrate single crystal formed in the petri dish. The incident polarization was changed using a half-wave plate. THF hydrates characteristics peak and ice transformation are visible only for the parallel configurations. (THF hydrate Raman shift = 922 cm^{-1}, Ice Raman shift = ~3150 cm^{-1})

3.2 Orientation of THF hydrates in Nanopores

The THF hydrates were formed in the AAO wafer with previously stated experimental procedure and observation. The angle-resolved experiments were performed by rotating the stage in a parallel configuration where the laser was polarized in the Y-direction. Raman signals were obtained experimentally at a predefined depth for a good signal-to-noise ratio. The data were acquired at two different locations in the same experiment, (i) at a location where hydrates were formed in the bulk of the microsystem; (ii) at a location where hydrates were formed inside the AAO nanopores. When the observed intensity for the rotation angle was plotted at these two locations, simple inspections (**Fig. 7**) clearly showed the effect of AAO nano-confinement on crystals. In the bulk of the microsystem, the obtained intensity values were almost constant irrespective of the rotation of the stage compared to intensity fluctuations when data was collected inside nanopores. Crystals formed in bulk and confinement can differ in kinetics, and kinetics can either be accelerated or suppressed completely by modifying the nanopores. Nano-confinement can affect the degree of crystallinity and lattice parameters too. This can be attributed to the specific orientations of the crystal inside nanopores compared to the random orientation in bulk.

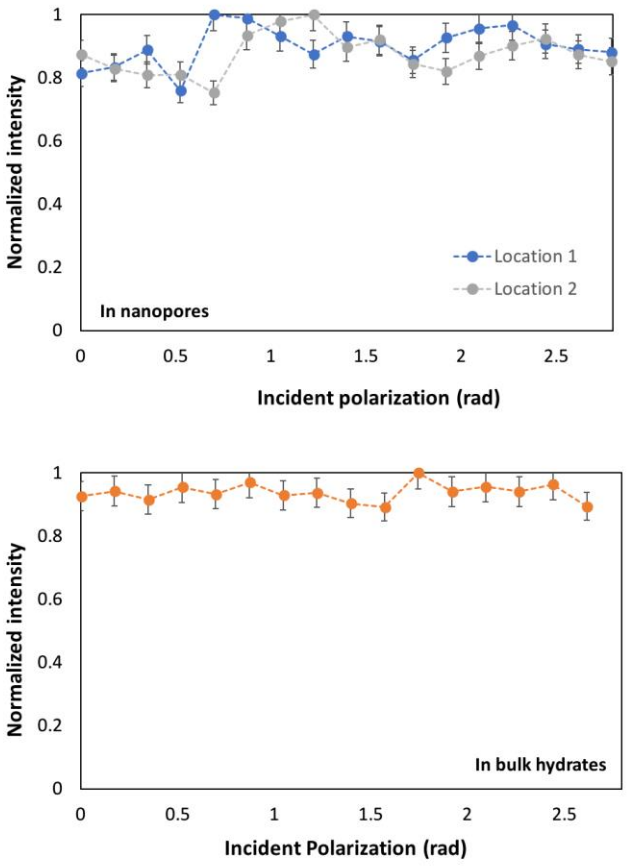

Figure 7. Normalized intensity values at 922 cm^{-1} for angle-resolved experiments in 20 nm diameter nanopores and in bulk hydrates

Intensity equations for curve fitting for F_{2g} modes can be written as

$$I_{\parallel} \propto ((a cos\psi sin\varphi + cos\varphi cos\theta sin\psi)^2 + a(cos\psi cos\varphi - cos\theta sin\psi sin\varphi)^2 + a sin\psi^2 sin\theta^2)^2 \qquad (14)$$

The obtained data were fitted using least square fit in MATLAB based on the equation generated using the formulations above, and crystal orientation was determined. The figure below shows the THF hydrates crystal orientation in the different pore diameters (**Fig. 8**).

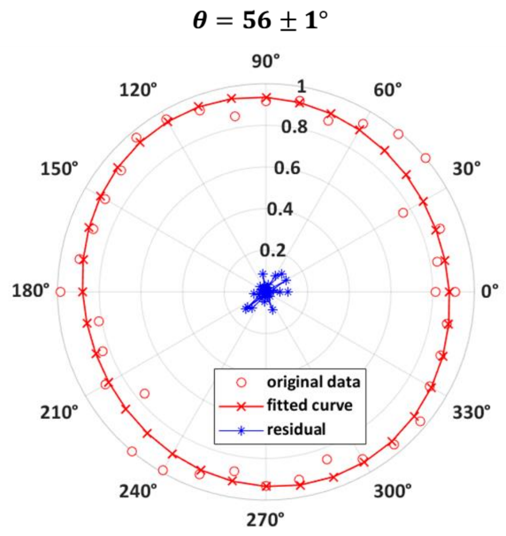

Pore diameter 20 nm

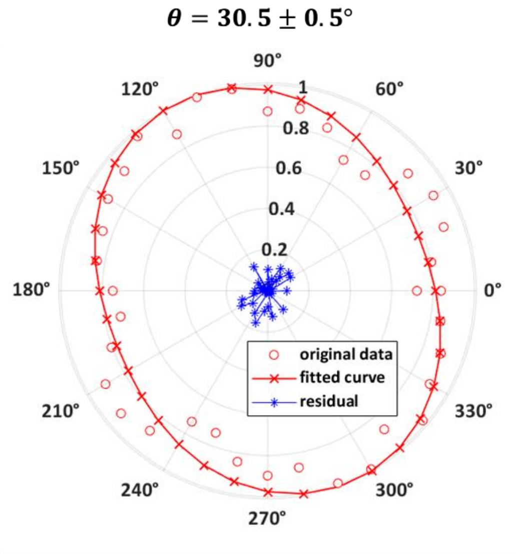

Pore diameter 40 nm

Figure 8. polar plots for the fitted intensity values using least square fit for 20 nm and 40 nm diameter nanopores

The fitted angles are φ = 2 ± 2, θ = 30.5 ± 0.5, ψ = 0 and φ = 0, θ = 56 ± 1, ψ = 159 ± 2 for 40nm and 20nm diameter pores, respectively. Here θ value is the tilt of the crystal inside with respect to the central axis of the nanopore, and other angles are the rotation of the crystal at its axis. For this study, we have chosen the conditions for forming the octahedral nature (symmetric) of the THF hydrate crystals. The rotation along its axis is of little importance in understanding the growth resulting preferred orientation of the crystals. However, it can be a separate study that would involve visualization experiments to understand if the tilt and rotation along the crystal axis influence the preferred crystal structure. Also, as the wavelength of the laser used in this study is much larger than the nanopores' diameter (785 nm vs 20, 40nm), it can be comprehended that the obtained tilt is the average tilt of the crystals in the region under focus. One implication of the obtained tilt is that crystals can grow much larger in higher-diameter nanopores than in smaller-diameter pores (**Fig. 11**). This implies that hydrate nucleation and growth mechanism can depend on the confinement size, which needs further exploration. However, polarized Raman spectroscopy cannot be used to determine crystal size. The length of the crystal can be theoretically calculated based on the obtained crystal tilt and the nanopores' diameter (assuming the crystals' octahedral nature).

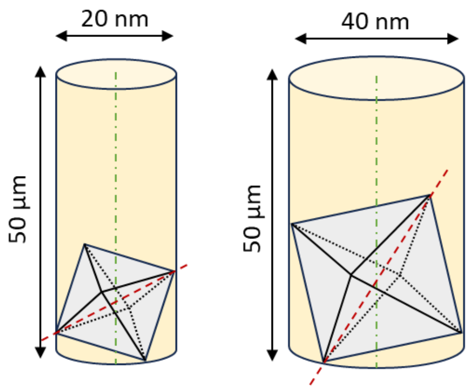

Figure 9. The sketch of the crystal tilt observed in 20 and 40 nm nanopores with reference to the pore axis

Confinement effects are important in controlling the properties of the materials confined in the nano spaces. As confinement leads to a larger proportion of material close to the confined surface, the effect largely depends on the surface-to-volume ratios; also, interfacial effects are often more important. Property changes usually are the effect of attraction or the repulsion dynamics between the material and the confinement. Nano-confinement can also help stabilize the different polymorphs of the material depending on the interaction, which can affect the growth rate and the observed properties, such as melting point. It has been shown in the literature that the tilt inside the confinement can have significant implications on the melting point of the crystal compared to the bulk of the system, which can be dictated by the Gibbs-Thomson equation[76, 77]. In a recent simulation study, researchers have shown that Gibbs Thomson equation correctly predicts the melting temperature depression under confinement for crystals. Understanding crystallization in confinement presents the opportunity to understand interaction between the crystal and confinement medium. The melting point is the indicator of the stability of the crystals. The change in melting point inside nanopores indicates a strong interaction between the crystal surface and the surface of the confinement medium. In general, changes in crystallization kinetics can be the reason for the observed depression in melting point resulting in slower growth with hindered nucleation. Some of the reasons for hindered nucleation are:

1. Nucleation is a stochastic process that requires ions to come together to form clusters. The probability of these clusters forming, even at large supersaturations, is decreased in smaller pores.
2. Surface chemistry influences crystallization within the pores.
3. Crystals with large surface-to-volume ratios can exhibit higher solubilities than their bulk counterparts, and a solution can simultaneously be undersaturated and supersaturated with respect to a crystal in small and large pores, respectively.
4. The growth of crystals via the aggregation of nanocrystal building blocks could potentially be retarded in small pores.

This can lead to a stage where the system is trapped in a thermodynamically unstable state for a long time. This is true for any system because intermediate unstable crystalline states should be passed before reaching a stable crystalline state. Based on the Gibbs-Thomson equation, the melting point usually decreases with the decrease in the pore size or the confinement medium. Calculating the melting point depression as per the equation requires the knowledge of the different parameters in which the crystal tilt plays a significant role in the melting point depression of the particle. This has to do with the interaction of the surface energies and the length of the crystals on the growth and stability of the crystals. The general Gibbs-Thomson equation is given below.

$$\frac{\Delta T_m(r)}{T_{m,bulk}} = -\frac{2M}{\Delta H^{fus}\rho r}\gamma_{nl}\cos\theta \qquad (15)$$

Here ρ is the crystal density, M is the molar mass, γ_{nl} is the surface tension between the crystal and the fluid surrounding it, θ is the interfacial angle between the condensed phase and the confined media on which it may have nucleated and ΔH^{fus} is the molar heat of fusion in bulk. Where nuclei do not wet the pore walls, the contact angle may be taken as 180^o; however, in the case of THF hydrates in AAO where AAO is hydrophilic, crystal tilt is crucial for calculating the melting point depression. After determining the tilt experimentally, the Gibbs-Thomson equation was used to calculate the melting point depression and based on the literature values of the data for other parameters and observed crystal tilt, the observed melting point depression is 1.6±0.01°C and 1.8±0.01°C compared to the bulk of the THF hydrates for 40 and 20 nm diameter pores respectively. Crystallization within AAO leads to a preferential orientation of crystals. This is due to the competitive growth effects where unimpeded growth is only possible parallel to the pore axis. When pores are comparable in diameter to the critical nucleus size, growth may be constrained such that crystals cannot exceed a critical volume, further promoting the growth of the highly oriented crystals. Which may affect the observed melting point compared to the bulk of the system.

The approach used for measuring the tilt is based on visual inspection for the formation of the hydrates. However, it was difficult to observe melting or crystallization inside the nanopores, the angular measurement was taken only when hydrates were visible on a bulk scale outside the nanopores. Also, obtaining systematic data regarding this effect can be extremely difficult since, knowledge of the pore-size distribution is critical to our understanding of the crystallization behaviour, where nanopores and macropores can drastically change the potential for crystallization in any pore size range. Also, the shape of the pores can influence crystallization and the solubility of the crystals must be considered. It is also difficult to determine where nucleation occurs within nanopores. While one might assume that the nucleation barrier is reduced on the pore wall, it is noted that crystallization within porous/confined media is often associated with the presence of a fluid layer between the crystal and the adjacent substrate.

As confinement effect depends on various parameters such as pore size distribution, shape, size, interconnectivity, solubility and composition of the system, the location where nucleation starts, and surface properties of crystals and wall of nanoconfinement, systems studied in literature cannot be directly compared. Detailed investigations about the melting point depression and kinetics inside the nanopores are part of another study and will be presented separately. However, depression was higher in smaller pores.

4 Conclusion

Understanding the gas hydrate nucleation and dissociation under confinement is crucial for developing hydrate technologies for a sustainable future. The potential of polarized Raman spectroscopy for understanding the THF hydrate crystal orientation in nano-confinement at low temperatures is shown for the first time. The proposed method is the first step toward understanding the effect of nano-confinement using non-invasive polarized Raman spectroscopy and microsystem for hydrate research. The technique shown here can also be used for a wide variety of systems that are not stable under atmospheric conditions. Cylindrical Anodic Aluminium Oxide nanopores of depth 50 µm and 20, 40 nm diameter were used as a nano-confinement where quality of the spectral resolution depends on the depth of focus, which was experimentally determined for each nanopore size. According to the polarized Raman theory and through single crystal studies, it was found that the determination of Raman tensor elements is not necessary for octahedral THF hydrate crystals. This is important to systems where the isolation of a single crystal is not possible to obtain reference values. Instrument configurations were carefully chosen to perform angle-resolved experiments to avoid hydrate dissociation during experiments. Angle-resolved experiments were performed in AAO oxide nanopores for formed THF hydrate crystals and average crystal tilt of 56±1° and 30.5±0.5° were observed for the 20nm and 40nm diameter pores, respectively. The obtained experimental evidence supports the dependence of the hydrate nucleation and growth mechanism on the confinement size, which requires further exploration regarding the kinetics and mechanism. The effect of crystal orientation on the properties of the crystal was explored in terms of the melting point depressions using the Gibbs-Thomson equation. The melting point depression calculated using the Gibbs-Thomson equation and measured crystal tilt shows a depression of 1.6-1.8°C in melting point compared to the bulk hydrates.

5 Author Contributions

The manuscript was written through the contributions of all authors. Conceptualization: R.L.H. and M.K.S Writing original draft: M.K.S, R.L.H and C.A.K; Experiments and data generation: M.K.S and X.N.L; Editing: M.K.S. and R.L.H. Corresponding: R.L.H. All authors have approved the final version of the manuscript.

Conflicts of interest

There are no conflicts to declare.

Acknowledgments

This work is supported by the U.S. Department of Energy, Office of Science, Office of Basic Energy Sciences Synthesis and Processing Science program under Award Number DE-SC-0022161. The authors thank Yuan Yan, Zoe Adkins, Lindsey Wadsworth, and Ahmad A. A. Majid for helpful discussions.

References

1. E. D. Sloan Jr, *Nature*, 2003, **426**, 353-359.
2. C. A. Koh, E. D. Sloan, A. K. Sum and D. T. Wu, *Annual review of chemical and biomolecular engineering*, 2011, **2**, 237-257.
3. C. A. Koh, *Chemical Society Reviews*, 2002, **31**, 157-167.
4. E. D. Sloan, *Energy & fuels*, 1998, **12**, 191-196.
5. Z. Yin and P. Linga, *Chinese Journal of Chemical Engineering*, 2019, **27**, 2026-2036.
6. P. Englezos and J. D. Lee, *Korean Journal of Chemical Engineering*, 2005, **22**, 671-681.
7. A. Demirbas, *Energy Conversion and Management*, 2010, **51**, 1547-1561.
8. K. A. Kvenvolden, *The future of energy gases*, 1993, **1570**, 279-291.
9. T. Collett, J.-J. Bahk, R. Baker, R. Boswell, D. Divins, M. Frye, D. Goldberg, J. Husebø, C. Koh and M. Malone, *Journal of chemical & engineering data*, 2015, **60**, 319-329.
10. C. P. Ribeiro Jr and P. L. Lage, *Chemical Engineering Science*, 2008, **63**, 2007-2034.
11. J. Zhang, S. Lee and J. W. Lee, *Industrial & Engineering Chemistry Research*, 2007, **46**, 6353-6359.

12. A. Vysniauskas and P. Bishnoi, *Chemical Engineering Science*, 1983, **38**, 1061-1072.
13. E. D. Sloan, S. Subramanian, P. Matthews, J. Lederhos and A. Khokhar, *Industrial & engineering chemistry research*, 1998, **37**, 3124-3132.
14. W. Ke, T. M. Svartaas and D. Chen, *Journal of Natural Gas Science and Engineering*, 2019, **61**, 169-196.
15. Z. Yin, M. Khurana, H. K. Tan and P. Linga, *Chemical Engineering Journal*, 2018, **342**, 9-29.
16. K. A. Kvenvolden and M. A. McMenamin, *Hydrates of natural gas: a review of their geologic occurrence*, United States Department of the Interior, Geological Survey, 1980.
17. M. C. Kennicutt, J. M. Brooks and H. B. Cox, *Organic Geochemistry: Principles and Applications*, 1993, 535-544.
18. C. Ruppel, *MITEI natural gas Report, supplementary paper on Methane Hydrates*, 2011, **4**, 1-25.
19. J. Wang and H. C. Lau, *Fuel*, 2020, **282**, 118784.
20. T. S. Collett, A. Johnson, C. C. Knapp and R. Boswell, *Natural gas hydrates: Energy resource potential and associated geologic hazards, AAPG Memoir 89*, AAPG, 2010.
21. C. D. Ruppel, *Nature Eduction Knowledge*, 2011, **2**, 12.
22. B. Tohidi, R. Anderson, M. B. Clennell, R. W. Burgass and A. B. Biderkab, *Geology*, 2001, **29**, 867-870.
23. J. Zhang, N. Zhang, X. Sun, J. Zhong, Z. Wang, L. Hou, S. Li and B. Sun, *Fuel*, 2023, **333**, 126312.
24. Y. Ji, J. Hou, E. Zhao, C. Liu, T. Guo, Y. Liu, B. Wei and Y. Bai, *Journal of Natural Gas Science and Engineering*, 2021, **95**, 104230.
25. X. Li, C. Wang, Q. Li, W. Pang, G. Chen and C. Sun, *Chemical Engineering Science*, 2022, **248**, 117227.
26. K. Nauhaus, A. Boetius, M. Krüger and F. Widdel, *Environmental microbiology*, 2002, **4**, 296-305.
27. G. Bohrmann, W. F. Kuhs, S. A. Klapp, K. S. Techmer, H. Klein, M. M. Murshed and F. Abegg, *Marine Geology*, 2007, **244**, 1-14.
28. Q. Sun, M. Du, X. Li, X. Guo, A. Liu, G. Chen and L. Yang, *Chemical Engineering Science*, 2019, **206**, 1-9.
29. Q. Sun, M. Du, X. Li, X. Guo and L. Yang, *Crystals*, 2019, **9**, 307.
30. A. Touil, D. Broseta and A. Desmedt, *Langmuir*, 2019, **35**, 12569-12581.
31. S.-P. Kang and J.-W. Lee, *The Journal of Physical Chemistry B*, 2010, **114**, 6973-6978.
32. C. Dicharry, C. Duchateau, H. Asbaï, D. Broseta and J.-P. Torré, *Chemical Engineering Science*, 2013, **98**, 88-97.
33. A. Kumar, B. Maini, P. Bishnoi, M. Clarke, O. Zatsepina and S. Srinivasan, *Journal of petroleum science and engineering*, 2010, **70**, 114-122.
34. D. WooáKim, *Physical Chemistry Chemical Physics*, 2014, **16**, 22717-22722.
35. J. Zhao, L. Yang, Y. Liu and Y. Song, *Physical Chemistry Chemical Physics*, 2015, **17**, 22632-22641.
36. D. Kim, Y.-H. Ahn, S.-J. Kim, J. Y. Lee, J. Lee, Y.-j. Seo and H. Lee, *The Journal of Physical Chemistry C*, 2015, **119**, 22148-22153.
37. F. Fontana, P. Figueiredo, P. Zhang, J. T. Hirvonen, D. Liu and H. A. Santos, *Advanced drug delivery reviews*, 2018, **131**, 3-21.
38. D. W. Moreau, *Ice Formation and Solvent Nanoconfinement in Protein Crystallography*, Cornell University, 2020.
39. J. Xu, S. Wang, G.-J. N. Wang, C. Zhu, S. Luo, L. Jin, X. Gu, S. Chen, V. R. Feig and J. W. To, *Science*, 2017, **355**, 59-64.
40. W. Hu, T. Cai, Y. Ma, J. K. Hobbs, O. Farrance and G. Reiter, *Faraday Discussions*, 2009, **143**, 129-141.
41. N. Winkler, M. Peterlechner and G. Wilde, *Journal of Materials Chemistry C*, 2015, **3**, 7543-7551.
42. Y. Leng and P. T. Cummings, *Physical review letters*, 2005, **94**, 026101.
43. M. A. Pimenta, G. C. Resende, H. B. Ribeiro and B. R. Carvalho, *Physical Chemistry Chemical Physics*, 2021, **23**, 27103-27123.
44. C.-Y. Chen, D. P. Wong, Y.-F. Huang, H.-T. Lien, P.-C. Chiang, P.-L. Li, F.-Y. Shih, W.-H. Wang, K.-H. Chen and L.-C. Chen, *ACS Photonics*, 2016, **3**, 985-991.
45. Y. Choi, K. Kim, S. Y. Lim, J. Kim, J. M. Park, J. H. Kim, Z. Lee and H. Cheong, *Nanoscale Horizons*, 2020, **5**, 308-315.
46. B. Zou, Y. Wei, Y. Zhou, D. Ke, X. Zhang, M. Zhang, C.-T. Yip, X. Chen, W. Li and H. Sun, *Nanoscale Horizons*, 2021, **6**, 809-818.
47. J. Wang, X. Luo, S. Li, I. Verzhbitskiy, W. Zhao, S. Wang, S. Y. Quek and G. Eda, *Advanced Functional Materials*, 2017, **27**, 1604799.
48. J. M. Benevides, S. A. Overman and G. J. Thomas Jr, *Journal of Raman Spectroscopy: An International Journal for Original Work in all Aspects of Raman Spectroscopy, Including Higher Order Processes, and also Brillouin and Rayleigh Scattering*, 2005, **36**, 279-299.
49. G. Duesberg, I. Loa, M. Burghard, K. Syassen and S. Roth, *Physical review letters*, 2000, **85**, 5436.
50. J. Kim, J.-U. Lee and H. Cheong, *Journal of Physics: Condensed Matter*, 2020, **32**, 343001.
51. J. Mossbrucker and T. Grotjohn, *Diamond and related materials*, 1996, **5**, 1333-1343.
52. G. Turrell, in *Practical Raman Spectroscopy*, eds. D. J. Gardiner and P. R. Graves, Springer Berlin Heidelberg, Berlin, Heidelberg, 1989, DOI: 10.1007/978-3-642-74040-4_2, pp. 13-54.
53. R. Loudon, *Advances in Physics*, 1964, **13**, 423-482.
54. R. Loudon, *Advances in Physics*, 2001, **50**, 813-864.
55. R. A. Heyler, J. T. Carriere and F. Havermeyer, 2013.
56. G. Hope, R. Woods and C. Munce, *Minerals Engineering*, 2001, **14**, 1565-1577.
57. A. R. Yadav and S. K. Mohite, *Asian Journal of Pharmacy and Technology*, 2020, **10**, 213-216.
58. M. M. Pyrch, L. J. Augustine, J. M. Williams, S. E. Mason and T. Z. Forbes, *Dalton Transactions*, 2022, **51**, 4772-4785.
59. M. Huang, H. Yan, C. Chen, D. Song, T. F. Heinz and J. Hone, *Proceedings of the National Academy of Sciences*, 2009, **106**, 7304-7308.
60. Y. Lan, M. Zondode, H. Deng, J.-A. Yan, M. Ndaw, A. Lisfi, C. Wang and Y.-L. Pan, *Crystals*, 2018, **8**, 375.
61. K. Ruschel, L. Nasdala, A. Kronz, J. M. Hanchar, D. M. Toebbens, R. Škoda, F. Finger and A. Möller, *Mineralogy and Petrology*, 2012, **105**, 41-55.
62. B. E. Scheetz and W. B. White, *Journal of the American Ceramic Society*, 1979, **62**, 468-470.
63. H. A. Stone and S. Kim, *American Institute of Chemical Engineers. AIChE Journal*, 2001, **47**, 1250.
64. Y. K. Suh and S. Kang, *Micromachines*, 2010, **1**, 82-111.
65. G. M. Whitesides, *nature*, 2006, **442**, 368-373.
66. J. Zhang, S. Yan, D. Yuan, G. Alici, N.-T. Nguyen, M. E. Warkiani and W. Li, *Lab on a Chip*, 2016, **16**, 10-34.

67. X. Li, C. Wang, S. Liang, X. Guo and Q. Sun, *Chemical Engineering Science*, 2020, **227**, 115937.
68. W. Chen, B. Pinho and R. L. Hartman, *Lab on a Chip*, 2017, **17**, 3051-3060.
69. S. Kawahata and M.-C. Deng, *International Journal of Automation and Computing*, 2016, **13**, 401-408.
70. J. Lee, T. Yun, J. Santamarina and C. Ruppel, *Geochemistry, Geophysics, Geosystems*, 2007, **8**.
71. W. Zhu and G. Pezzotti, *physica status solidi (a)*, 2011, **208**, 1141-1150.
72. C. Tulk, D. Klug and J. Ripmeester, *The Journal of Physical Chemistry A*, 1998, **102**, 8734-8739.
73. B. I. Swanson, *Applied Spectroscopy*, 1973, **27**, 382-385.
74. L.-l. Jiang, Y.-f. Song, W.-l. Liu, H.-l. Wu, X.-y. Li and Y.-q. Yang, *Chemical Physics Letters*, 2021, **765**, 138256.
75. Y. Takasu, S. Matsumoto, Y. Fujii and I. Nishio, *Chemical Physics Letters*, 2015, **627**, 39-43.
76. G. Höhne, *Polymer*, 2002, **43**, 4689-4698.
77. L. Scalfi, B. Coasne and B. Rotenberg, *The Journal of Chemical Physics*, 2021, **154**, 114711.